

# UC Riverside

## UC Riverside Previously Published Works

### Title

GPU accelerated real-time multi-functional spectral-domain optical coherence tomography system at 1300nm

### Permalink

<https://escholarship.org/uc/item/2gd1m3tb>

### Journal

Optics Express, 20(14)

### ISSN

1094-4087

### Authors

Wang, Yan  
Oh, Christian M  
Oliveira, Michael C  
[et al.](#)

### Publication Date

2012-07-02

### DOI

10.1364/oe.20.014797

Peer reviewed

# GPU accelerated real-time multi-functional spectral-domain optical coherence tomography system at 1300nm

Yan Wang, Christian M. Oh, Michael C. Oliveira, M. Shahidul Islam, Arthur Ortega, and B. Hyle Park\*

Department of Bioengineering, University of California, Riverside, 900 University Ave., Riverside, CA 92521, USA  
\*hylepark@engr.ucr.edu

**Abstract:** We present a GPU accelerated multi-functional spectral domain optical coherence tomography system at 1300nm. The system is capable of real-time processing and display of every intensity image, comprised of 512 pixels by 2048 A-lines acquired at 20 frames per second. The update rate for all four images with size of 512 pixels by 2048 A-lines simultaneously (intensity, phase retardation, flow and *en face* view) is approximately 10 frames per second. Additionally, we report for the first time the characterization of phase retardation and diattenuation by a sample comprised of a stacked set of polarizing film and wave plate. The calculated optic axis orientation, phase retardation and diattenuation match well with expected values. The speed of each facet of the multi-functional OCT CPU-GPU hybrid acquisition system, intensity, phase retardation, and flow, were separately demonstrated by imaging a horseshoe crab lateral compound eye, a non-uniformly heated chicken muscle, and a microfluidic device. A mouse brain with thin skull preparation was imaged *in vivo* and demonstrated the capability of the system for live multi-functional OCT visualization.

©2012 Optical Society of America

**OCIS codes:** (170.4500) Optical coherence tomography; (170.3880) Medical and biological imaging; (260.1440) Birefringence; (230.5440) Polarization-selective devices; (280.2490) Flow diagnostics; (200.4560) Optical data processing.

---

## References and links

1. D. Huang, E. A. Swanson, C. P. Lin, J. S. Schuman, W. G. Stinson, W. Chang, M. R. Hee, T. Flotte, K. Gregory, C. A. Puliafito, and J. G. Fujimoto, "Optical Coherence Tomography," *Science* **254**(5035), 1178–1181 (1991).
2. T. Mitsui, "Dynamic range of optical reflectometry with spectral interferometry," *Jpn. J. Appl. Phys.* **38**(Part 1, No. 10), 6133–6137 (1999).
3. R. Leitgeb, C. K. Hitzenberger, and A. F. Fercher, "Performance of fourier domain vs. time domain optical coherence tomography," *Opt. Express* **11**(8), 889–894 (2003).
4. J. F. de Boer, B. Cense, B. H. Park, M. C. Pierce, G. J. Tearney, and B. E. Bouma, "Improved signal-to-noise ratio in spectral-domain compared with time-domain optical coherence tomography," *Opt. Lett.* **28**(21), 2067–2069 (2003).
5. M. A. Choma, M. V. Sarunic, C. H. Yang, and J. A. Izatt, "Sensitivity advantage of swept source and Fourier domain optical coherence tomography," *Opt. Express* **11**(18), 2183–2189 (2003).
6. M. R. Hee, J. A. Izatt, E. A. Swanson, D. Huang, J. S. Schuman, C. P. Lin, C. A. Puliafito, and J. G. Fujimoto, "Optical coherence tomography of the human retina," *Arch. Ophthalmol.* **113**(3), 325–332 (1995).
7. W. Drexler, U. Morgner, R. K. Ghanta, F. X. Kärtner, J. S. Schuman, and J. G. Fujimoto, "Ultrahigh-resolution ophthalmic optical coherence tomography," *Nat. Med.* **7**(4), 502–507 (2001).
8. M. Wojtkowski, R. Leitgeb, A. Kowalczyk, T. Bajraszewski, and A. F. Fercher, "In vivo human retinal imaging by Fourier domain optical coherence tomography," *J. Biomed. Opt.* **7**(3), 457–463 (2002).
9. B. Cense, N. A. Nassif, T. Chen, M. Pierce, S. H. Yun, B. H. Park, B. E. Bouma, G. J. Tearney, and J. F. de Boer, "Ultrahigh-resolution high-speed retinal imaging using spectral-domain optical coherence tomography," *Opt. Express* **12**(11), 2435–2447 (2004).

10. G. Wollstein, J. S. Schuman, L. L. Price, A. Aydin, S. A. Beaton, P. C. Stark, J. G. Fujimoto, and H. Ishikawa, "Optical coherence tomography (OCT) macular and peripapillary retinal nerve fiber layer measurements and automated visual fields," *Am. J. Ophthalmol.* **138**(2), 218–225 (2004).
11. J. Welzel, E. Lankenau, R. Birngruber, and R. Engelhardt, "Optical coherence tomography of the human skin," *J. Am. Acad. Dermatol.* **37**(6), 958–963 (1997).
12. M. C. Pierce, J. Strasswimmer, B. H. Park, B. Cense, and J. F. de Boer, "Advances in optical coherence tomography imaging for dermatology," *J. Invest. Dermatol.* **123**(3), 458–463 (2004).
13. T. Gambichler, G. Moussa, M. Sand, D. Sand, P. Altmeyer, and K. Hoffmann, "Applications of optical coherence tomography in dermatology," *J. Dermatol. Sci.* **40**(2), 85–94 (2005).
14. J. G. Fujimoto, M. E. Brezinski, G. J. Tearney, S. A. Boppart, B. Bouma, M. R. Hee, J. F. Southern, and E. A. Swanson, "Optical biopsy and imaging using optical coherence tomography," *Nat. Med.* **1**(9), 970–972 (1995).
15. A. M. Rollins, S. Yazdanfar, M. Kulkarni, R. Ung-Arunyawee, and J. A. Izatt, "In vivo video rate optical coherence tomography," *Opt. Express* **3**(6), 219–229 (1998).
16. S. A. Boppart, M. E. Brezinski, and J. G. Fujimoto, "Optical coherence tomography imaging in developmental biology," *Methods Mol. Biol.* **135**, 217–233 (2000).
17. P. O. Bagnaninchi, Y. Yang, N. Zghoul, N. Maffulli, R. K. Wang, and A. J. Haj, "Chitosan microchannel scaffolds for tendon tissue engineering characterized using optical coherence tomography," *Tissue Eng.* **13**(2), 323–331 (2007).
18. J. G. Fujimoto, S. A. Boppart, G. J. Tearney, B. E. Bouma, C. Pitris, and M. E. Brezinski, "High resolution in vivo intra-arterial imaging with optical coherence tomography," *Heart* **82**(2), 128–133 (1999).
19. I. K. Jang, B. E. Bouma, D. H. Kang, S. J. Park, S. W. Park, K. B. Seung, K. B. Choi, M. Shishkov, K. Schlendorf, E. Pomerantsev, S. L. Houser, H. T. Aretz, and G. J. Tearney, "Visualization of coronary atherosclerotic plaques in patients using optical coherence tomography: comparison with intravascular ultrasound," *J. Am. Coll. Cardiol.* **39**(4), 604–609 (2002).
20. B. E. Bouma, G. J. Tearney, H. Yabushita, M. Shishkov, C. R. Kauffman, D. DeJoseph Gauthier, B. D. MacNeill, S. L. Houser, H. T. Aretz, E. F. Halpern, and I. K. Jang, "Evaluation of intracoronary stenting by intravascular optical coherence tomography," *Heart* **89**(3), 317–320 (2003).
21. W. Luo, D. L. Marks, T. S. Ralston, and S. A. Boppart, "Three-dimensional optical coherence tomography of the embryonic murine cardiovascular system," *J. Biomed. Opt.* **11**(2), 021014 (2006).
22. Z. Chen, T. E. Milner, D. Dave, and J. S. Nelson, "Optical Doppler tomographic imaging of fluid flow velocity in highly scattering media," *Opt. Lett.* **22**(1), 64–66 (1997).
23. J. A. Izatt, M. D. Kulkarni, S. Yazdanfar, J. K. Barton, and A. J. Welch, "In vivo bidirectional color Doppler flow imaging of picoliter blood volumes using optical coherence tomography," *Opt. Lett.* **22**(18), 1439–1441 (1997).
24. T. G. van Leeuwen, M. D. Kulkarni, S. Yazdanfar, A. M. Rollins, and J. A. Izatt, "High-flow-velocity and shear-rate imaging by use of color Doppler optical coherence tomography," *Opt. Lett.* **24**(22), 1584–1586 (1999).
25. Y. Zhao, Z. Chen, C. Saxer, S. Xiang, J. F. de Boer, and J. S. Nelson, "Phase-resolved optical coherence tomography and optical Doppler tomography for imaging blood flow in human skin with fast scanning speed and high velocity sensitivity," *Opt. Lett.* **25**(2), 114–116 (2000).
26. Y. Zhao, Z. Chen, C. Saxer, Q. Shen, S. Xiang, J. F. de Boer, and J. S. Nelson, "Doppler standard deviation imaging for clinical monitoring of in vivo human skin blood flow," *Opt. Lett.* **25**(18), 1358–1360 (2000).
27. B. R. White, M. C. Pierce, N. Nassif, B. Cense, B. H. Park, G. J. Tearney, B. E. Bouma, T. C. Chen, and J. F. de Boer, "In vivo dynamic human retinal blood flow imaging using ultra-high-speed spectral domain optical coherence tomography," *Opt. Express* **11**(25), 3490–3497 (2003).
28. N. A. Nassif, B. Cense, B. H. Park, M. C. Pierce, S. H. Yun, B. Bouma, G. J. Tearney, T. C. Chen, and J. F. de Boer, "In vivo high-resolution video-rate spectral-domain optical coherence tomography of the human retina and optic nerve," *Opt. Express* **12**(3), 367–376 (2004).
29. M. R. Hee, D. Huang, E. A. Swanson, and J. G. Fujimoto, "Polarization-sensitive low-coherence reflectometer for birefringence characterization and ranging," *J. Opt. Soc. Am. B* **9**(6), 903–909 (1992).
30. J. F. de Boer, T. E. Milner, M. J. C. van Gemert, and J. S. Nelson, "Two-dimensional birefringence imaging in biological tissue by polarization-sensitive optical coherence tomography," *Opt. Lett.* **22**(12), 934–936 (1997).
31. J. F. de Boer, T. E. Milner, and J. S. Nelson, "Determination of the depth-resolved Stokes parameters of light backscattered from turbid media by use of polarization-sensitive optical coherence tomography," *Opt. Lett.* **24**(5), 300–302 (1999).
32. B. H. Park, C. Saxer, S. M. Srinivas, J. S. Nelson, and J. F. de Boer, "In vivo burn depth determination by high-speed fiber-based polarization sensitive optical coherence tomography," *J. Biomed. Opt.* **6**(4), 474–479 (2001).
33. S. M. Srinivas, J. F. de Boer, H. Park, K. Keikhanzadeh, H. E. Huang, J. Zhang, W. Q. Jung, Z. Chen, and J. S. Nelson, "Determination of burn depth by polarization-sensitive optical coherence tomography," *J. Biomed. Opt.* **9**(1), 207–212 (2004).
34. M. C. Pierce, R. L. Sheridan, B. Hyle Park, B. Cense, and J. F. de Boer, "Collagen denaturation can be quantified in burned human skin using polarization-sensitive optical coherence tomography," *Burns* **30**(6), 511–517 (2004).
35. B. Cense, T. C. Chen, B. H. Park, M. C. Pierce, and J. F. de Boer, "In vivo depth-resolved birefringence measurements of the human retinal nerve fiber layer by polarization-sensitive optical coherence tomography," *Opt. Lett.* **27**(18), 1610–1612 (2002).

36. B. Cense, T. C. Chen, B. H. Park, M. C. Pierce, and J. F. de Boer, "In vivo birefringence and thickness measurements of the human retinal nerve fiber layer using polarization-sensitive optical coherence tomography," *J. Biomed. Opt.* **9**(1), 121–125 (2004).
37. D. Fried, J. Xie, S. Shafi, J. D. B. Featherstone, T. M. Breunig, and C. Le, "Imaging caries lesions and lesion progression with polarization sensitive optical coherence tomography," *J. Biomed. Opt.* **7**(4), 618–627 (2002).
38. A. Baumgartner, S. Dichtl, C. K. Hitzberger, H. Sattmann, B. Robl, A. Moritz, A. F. Fercher, and W. Sperr, "Polarization-sensitive optical coherence tomography of dental structures," *Caries Res.* **34**(1), 59–69 (2000).
39. S. K. Nadkarni, M. C. Pierce, B. H. Park, J. F. de Boer, P. Whittaker, B. E. Bouma, J. E. Bressner, E. Halpern, S. L. Houser, and G. J. Tearney, "Measurement of collagen and smooth muscle cell content in atherosclerotic plaques using polarization-sensitive optical coherence tomography," *J. Am. Coll. Cardiol.* **49**(13), 1474–1481 (2007).
40. W. C. Kuo, M. W. Hsiung, J. J. Shyu, N. K. Chou, and P. N. Yang, "Assessment of arterial characteristics in human atherosclerosis by extracting optical properties from polarization-sensitive optical coherence tomography," *Opt. Express* **16**(11), 8117–8125 (2008).
41. M. C. Pierce, B. Hyle Park, B. Cense, and J. F. de Boer, "Simultaneous intensity, birefringence, and flow measurements with high-speed fiber-based optical coherence tomography," *Opt. Lett.* **27**(17), 1534–1536 (2002).
42. H. Ren, Z. Ding, Y. Zhao, J. Miao, J. S. Nelson, and Z. Chen, "Phase-resolved functional optical coherence tomography: simultaneous imaging of *in situ* tissue structure, blood flow velocity, standard deviation, birefringence, and Stokes vectors in human skin," *Opt. Lett.* **27**(19), 1702–1704 (2002).
43. B. H. Park, M. C. Pierce, B. Cense, and J. F. de Boer, "Real-time multi-functional optical coherence tomography," *Opt. Express* **11**(7), 782–793 (2003).
44. B. H. Park, M. C. Pierce, B. Cense, S. Yun, M. Mujat, G. J. Tearney, B. E. Bouma, and J. F. de Boer, "Real-time fiber-based multi-functional spectral-domain optical coherence tomography at 1.3  $\mu\text{m}$ ," *Opt. Express* **13**(11), 3931–3944 (2005).
45. L. An, P. Li, T. T. Shen, and R. Wang, "High speed spectral domain optical coherence tomography for retinal imaging at 500,000 A-lines per second," *Biomed. Opt. Express* **2**(10), 2770–2783 (2011).
46. T. Bonin, G. Franke, M. Hagen-Eggert, P. Koch, and G. Hüttmann, "In vivo Fourier-domain full-field OCT of the human retina with 1.5 million A-lines/s," *Opt. Lett.* **35**(20), 3432–3434 (2010).
47. T. E. Ustun, N. V. Iftimia, R. D. Ferguson, and D. X. Hammer, "Real-time processing for Fourier domain optical coherence tomography using a field programmable gate array," *Rev. Sci. Instrum.* **79**(11), 114301 (2008).
48. A. E. Desjardins, B. J. Vakoc, M. J. Suter, S. H. Yun, G. J. Tearney, and B. E. Bouma, "Real-time FPGA processing for high-speed optical frequency domain imaging," *IEEE Trans. Med. Imaging* **28**(9), 1468–1472 (2009).
49. Y. Watanabe and T. Itagaki, "Real-time display on Fourier domain optical coherence tomography system using a graphics processing unit," *J. Biomed. Opt.* **14**(6), 060506 (2009).
50. S. Van der Jeught, A. Bradu, and A. G. Podoleanu, "Real-time resampling in Fourier domain optical coherence tomography using a graphics processing unit," *J. Biomed. Opt.* **15**(3), 030511 (2010).
51. K. Zhang and J. U. Kang, "Real-time 4D signal processing and visualization using graphics processing unit on a regular nonlinear-k Fourier-domain OCT system," *Opt. Express* **18**(11), 11772–11784 (2010).
52. J. Rasakanthan, K. Sugden, and P. H. Tomlins, "Processing and rendering of Fourier domain optical coherence tomography images at a line rate over 524 kHz using a graphics processing unit," *J. Biomed. Opt.* **16**(2), 020505 (2011).
53. NVIDIA, "NVIDIA CUDA Compute Unified Device Architecture Programming Guide Version 4.0," (2011).
54. NVIDIA, "NVIDIA CUDA CUFFT Library Version 4.0," (2011).
55. M. Mujat, B. H. Park, B. Cense, T. C. Chen, and J. F. de Boer, "Autocalibration of spectral-domain optical coherence tomography spectrometers for in vivo quantitative retinal nerve fiber layer birefringence determination," *J. Biomed. Opt.* **12**(4), 041205 (2007).
56. S. H. Yun, G. J. Tearney, B. E. Bouma, B. H. Park, and J. F. de Boer, "High-speed spectral-domain optical coherence tomography at 1.3  $\mu\text{m}$  wavelength," *Opt. Express* **11**(26), 3598–3604 (2003).
57. B. H. Park, M. C. Pierce, B. Cense, and J. F. de Boer, "Jones matrix analysis for a polarization-sensitive optical coherence tomography system using fiber-optic components," *Opt. Lett.* **29**(21), 2512–2514 (2004).
58. E. Fischer, "Birefringence and ultrastructure of muscle," *Ann. N. Y. Acad. Sci.* **47**(6 Art 6), 783–797 (1947).
59. R. W. Cox, "Hibernoma": The lipoma of immature adipose tissue," *J. Pathol. Bacteriol.* **68**(2), 511–518 (1954).
60. M. Bonesi, D. Y. Churmakov, L. J. Ritchie, and I. V. Meglinski, "Turbulence monitoring with Doppler optical coherence tomography," *Laser Phys. Lett.* **4**(4), 304–307 (2007).

---

## 1. Introduction

Optical coherence tomography (OCT) is an optical imaging method based on low-coherence interferometry capable of high-resolution cross-sectional imaging of internal microstructure by measuring light backscattered from the sample [1]. Traditional time-domain OCT systems obtain depth-profiles (A-lines) of the sample using a moving reference arm. The emergence of second-generation systems of both spectral-domain and swept source types allows for increases in both line acquisition rate and sensitivity by several orders of magnitude compared

to their time-domain counterparts [2–5]. OCT has the capacity to perform non-contact, non-invasive *in vivo* imaging and has been applied in medical and scientific fields such as ophthalmology [6–10], dermatology [11–13], developmental biology [14–17], and cardiology [18–21].

Extensions of OCT such as Doppler OCT and polarization-sensitive OCT (PS-OCT) provide additional information about biological tissues. Doppler OCT combines the Doppler principle with OCT to obtain high-resolution tomographic images of simultaneous tissue structure and blood flow [22]. Bi-directional flow and phase variance can be calculated by observing the phase difference between successive depth profiles and this phase difference squared [23–28]. PS-OCT combines polarization sensitive detection with OCT to determine tissue birefringence [29–31]. PS-OCT has been used for imaging a variety of tissues, including thermal injury [32–34], retinal nerve fiber layer [35,36], caries lesions [37], dental structures [38], and human atherosclerosis [39,40]. A multi-functional SD-OCT system including intensity OCT, Doppler OCT and PS-OCT enables simultaneous acquisition of structure, flow and phase retardation information of tissue [41–44]. Advances in hardware have enabled line acquisition rates of 500 kHz for spectrometer-based OCT systems [45] and 1.5 million Hz for swept-source OCT systems [46]. However, the heavy computational load required to process the acquired data stream creates a bottleneck in the realization of real-time OCT, especially multi-functional OCT imaging [41–44, 47–50].

Rapid visualization allows for quick identification of different features of biological samples in any of the three image types (intensity, Doppler, and polarization-sensitive) during acquisition. Beyond OCT intensity image processing, which involves spectral resampling, interpolation and a fast Fourier transform (FFT), performing multi-functional OCT imaging demands additional processing for reconstruction of both PS-OCT and Doppler OCT images, further increasing the total processing time. One method to decrease the processing time is to exploit the inherent parallelism of graphics processing units (GPU). It has been demonstrated previously that an A-line processing rate of 680,000 A-scan/s can be achieved using GPU implementations of linear spline interpolation and the FFT [51]. A processing rate of 720,000 A-scan/s could be achieved by using GPU paged memory to render data in the GPU rather than copying back to CPU [52]. However, GPU implementations of PS-OCT and Doppler OCT processing algorithms have yet to be demonstrated. A multi-functional OCT imaging system would allow rapid visualization of biological samples with enhanced contrast, allowing the user to scan samples quickly for features of interest to image.

In this paper, we present a multi-functional SD-OCT system with real-time GPU processing capable of displaying simultaneous intensity, phase retardation, flow and *en face* images with size of 512 pixels by 2048 A-lines at a rate of 10 frames per second. Diattenuation and phase retardation characterization were accomplished using a combined polarizing film and wave plate sample. Finally, we demonstrate the acquisition and processing speed of the system by imaging of a horseshoe crab eye *in vivo*, non-uniformly heated chicken muscle, microfluidic device and mouse brain *in vivo*.

## 2. System and methods

### 2.1 Experimental setup

A schematic of the multi-functional SD-OCT system is shown in Fig. 1. The broadband source is composed of two super-luminescent diodes (SLD), one centered at 1295nm with a full-width at half maximum (FWHM) bandwidth of 97nm (Thorlabs Inc.) and the other centered at 1350nm with a FWHM bandwidth of 48nm (Denselight Semiconductors Pte Ltd). The resulting source is centered at 1298nm with a 120 nm FWHM bandwidth and 16mW power. Light from the source is collimated and passes through a polarization beam splitter (pbs) and a polarization modulator (pm, Thorlabs Inc.) that toggles the light between two orthogonal polarization states in a Poincare sphere representation. The polarized light is sent

to a fiber circulator (Thorlabs Inc.) and an 80/20 fiber splitter (AC Photonics Inc) with a polarization controller (pc). In the reference arm, a neutral density filter (ndf) is used to adjust light reflecting from reference mirror, and a polarizer (pl) is used to insure uniformity of the reference polarization state. In the sample arm, galvanometer mounted mirrors in the hand-piece provide transverse scanning of a 10 micron diameter focused spot. Light from both arms is recombined at the splitter and passes through a transmission diffraction grating (1100 lines per mm, Wasatch Photonics) before being focused by a planoconvex lens. The two polarization states of light are separated by a polarization beam splitter, and collected by two line scanning cameras (lsc, Goodrich SUI SU-LDH linear digital high speed InGaAs camera) separately with readout rates up to 45 kHz. Output from the two cameras is digitized through two National Instruments boards (PCIeNI-1429). The cameras, galvanometer mirrors and polarization modulator are triggered by synchronized signals sent from the computer via the National Instruments PCIe6259 board. The GPU used for data processing is the NVIDIA Tesla C1060 card, which is also connected via PCI express 2.0 x16 interface. This GPU card has 240 cores with core clock speed of 1.296 GHz, 4GB physical memory and memory clock speed of 800 MHz. The computer CPU is an Intel Xeon W5580, which has two cores with clock speed of 3.2 GHz.

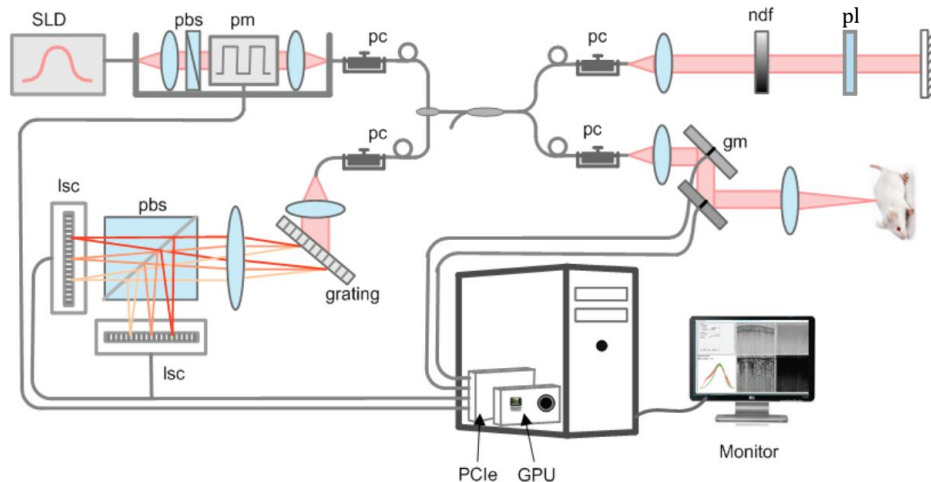


Fig. 1. Scheme of multi-functional SD-OCT system with GPU assisted processing

## 2.2 Acquisition and processing program

The real-time acquisition program was written in Visual C++ in Microsoft Visual Studio 2008, similar to the program written in previous SD-OCT system [44], but with significant modifications to the basic thread structure to accommodate GPU processing. The multi-threaded program synchronizes the cameras, galvanometer-mounted-mirrors and polarization modulator. In the meantime, one thread saves all the acquired data into a specified folder while another thread processes the raw data and displays the appropriate images on the different views in the graphical user interface (GUI). The thread responsible for processing the raw data controls the data transfer to and from the GPU, as well as the kernel invocations required for GPU processing of the different views (intensity, Doppler, and polarization-sensitive imaging).

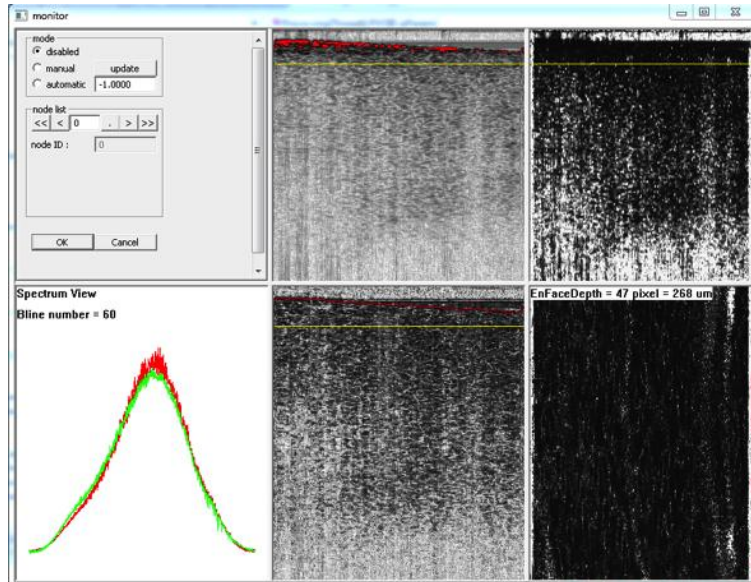


Fig. 2. Snap-shot of the GUI of the real-time data acquisition program during imaging of a mouse brain with a thin skull preparation. The control panel, indicating processing status, is shown at top left. The other five views are of the unprocessed spectra of the two cameras (bottom left), an intensity image (top middle), flow image (top right), polarization image (bottom middle) and *en face* flow image (bottom right). The yellow horizontal line in intensity, flow and polarization images indicate the depth of the *en face* image.

The GUI is comprised of five views with a sixth panel that shows program status (Fig. 2). The spectra of the two cameras are shown at the bottom left (the red and green spectra distinguish the two cameras), top middle and bottom middle display the intensity image and the phase retardation image respectively, and the top right and bottom right display the flow image and *en face* reconstruction. The red spots in the intensity image indicate regions in which the SNR exceeds a pre-specified range, the yellow line in intensity, polarization and flow images indicate the depth of *en face* reconstruction, which can be toggled between the different views. The pixel number and approximate physical depth of the *en face* view is also shown in upper left corner of *en face* view. The sizes of the image views on the GUI were scaled reflect the physical size of the scanned region of the sample (2mm by 2mm). The position and size of the four image views can be adjusted depending on lateral scan width and user preference. The imaged sample in Fig. 2 was a mouse brain with a thin skull preparation (2048A-lines  $\times$  200 frames  $\times$  512 points in depth, 2mm  $\times$  2mm  $\times$  2mm).

Figure 3 is a flowchart of the data flow through the hybrid CPU-GPU processing scheme in the acquisition software. The GPU was programmed using NVIDIA's Compute Unified Device Architecture (CUDA) [53]. Pre-calculation for wavelength-to-wavenumber resampling and loading of the calibration files for this interpolation are both done during software initialization on the CPU. Raw data with size of 1024 pixels by 2048 A-lines was converted from 16 bit unsigned integers into 32 bit floats on the CPU, and then copied to the GPU for processing. In GPU memory, the averaged spectrum was first calculated for each polarization state and then subtracted from the appropriate spectra. Next, linear interpolation was performed. Interpolation parameters differ between the two polarization channels. The gray boxes in Fig. 3 from the "resampled k" to "interpolation" steps indicate that two instances of the same thread logic with these different parameters were run separately. FFT operation was implemented using the CUFFT library provided by NVIDIA [54] identically for both channels. The data from these two channels was combined in a secondary processing step, which consisted of dB conversion and gray-scale encoding for intensity image display. The phase encoded by the complex result after FFT was used to calculate both phase

retardation and flow, details of which are described in sections 2.3.2 and 2.3.3, respectively. Next, bitmap encoding for both phase retardation and flow images was performed. The phase retardation values are encoded into an 8-bit gray scale color map, in which 0 and 180 degrees are represented by black and white respectively. The flow phase variance values are encoded in a similar color map, with zero and  $\pi^2$  represented by black and white respectively. Finally, an *en face* image is generated based on the desired image type (intensity, phase retardation or flow) by choosing a depth in an image and fetching the appropriate data from that depth in sequentially acquired cross-sectional images. The intensity (512 pixels by 2048 A-lines), phase retardation (512 pixels by 1024 A-lines), flow (512 pixels by 2046 A-lines) and *en face* (100 images by 2048 A-lines) bitmaps are then all copied back from GPU memory to CPU memory for display. The 2-D images (intensity, flow, phase retardation) display cross-sectional images of sample while the *en face* view displays a top-down view of the sample. Choosing the type of *en face* image and depth is done via a mouse click on any of the cross-sectional viewing frames in the GUI.

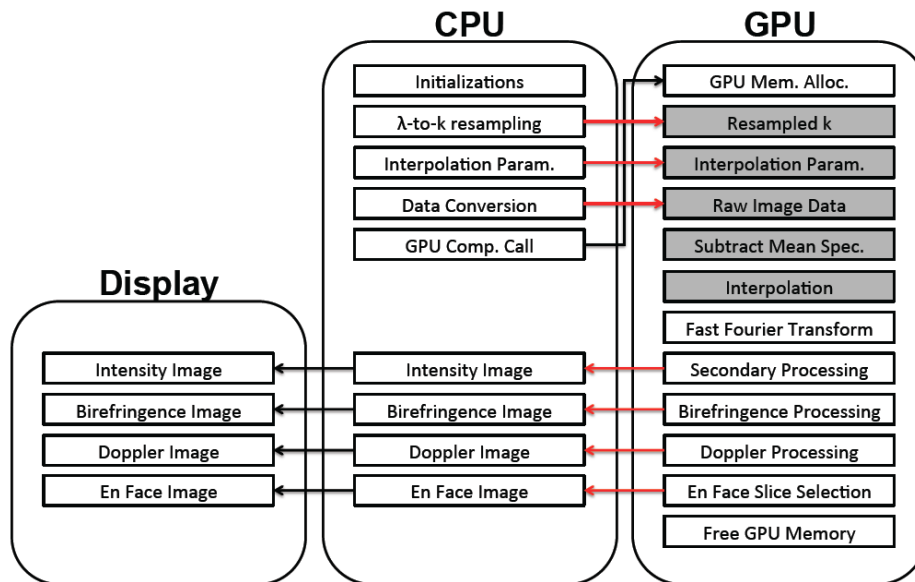


Fig. 3. Flowchart of the computation and image display of the hybrid CPU/GPU processing scheme in the program.

All image frames have 512 pixels in depth. The intensity, phase retardation and flow images have 2048, 1024 and 2046 A-lines respectively. The update rate for all the displays using strictly CPU processing is 2 frames per second. In the previous CPU version multi-threaded program, a main processing thread computed intensity image, then sent data after FFT done by using Intel Performance Primitives (IPP) to two threads to compute phase retardation and flow information separately. We see a 5x increase in the update rate to 10 frames per second when processing is performed on the GPU on the same computer.

A breakdown of the processing times for CPU and GPU processing is displayed in Table 1. It is clear that using a GPU to perform the computation necessary to reconstruct the three image types is faster compared to CPU processing. The total GPU processing and display time is 5 times faster than its CPU counterpart, despite the fact that 20% of the total time is used to transfer the data to and from the GPU. The effective A-line processing rate for intensity imaging only is 61 kHz. Newer versions of CUDA improve the use of pinned memory and execution of multiple kernels concurrently, which may help reduce the total computation time even further. Using pinned memory is theoretically possible to help reduce the data copying time between CPU and GPU by several milliseconds for our data size [52].



However, a significant improvement is still demonstrated here using GPU-CPU hybrid processing compared to CPU processing.

**Table 1. Time comparison of CPU and GPU calculation**

Task	CPU time (ms)	GPU time (ms)
Copy from buffer to CPU	12	12
Copy between CPU and GPU	0	22
Calculate intensity	55	10
Calculate phase retardation	392	25
Calculate flow	549	12
Display	25	25
Total	549	106

To determine the minimum number of A-lines per image required to see an improvement using GPU to process intensity only and multi-functional images, we compared the total time to process and display a single frame using the purely CPU and CPU-GPU hybrid programs respectively, while varying the number of A-lines (Fig. 4).

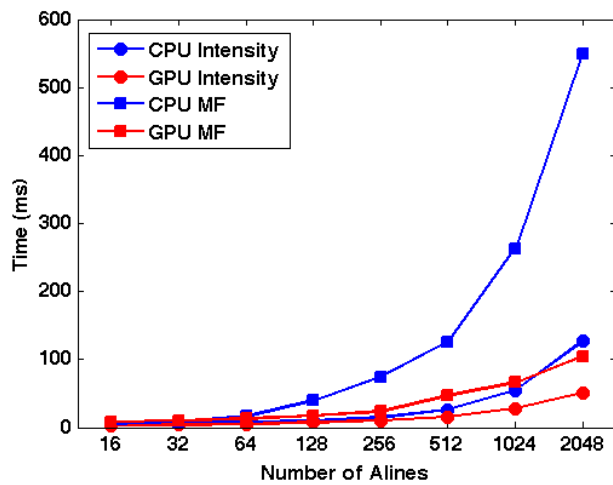


Fig. 4. Time comparison of CPU and GPU computation of intensity image only and multi-functional images at different number of A-lines.

The time difference between CPU and CPU-GPU processing of only intensity images increases as number of A-lines increases, indicating that GPU processing has an obvious advantage when processing larger amounts of data. The bulk of the GPU processing advantage come from the parallel implementation of the FFT. The time required to perform the FFT does not significantly increase with data size due to the efficient parallelization of different A-lines over the GPU cores. The time difference of computing all intensity, phase retardation and flow images by purely CPU and CPU-GPU hybrid programs increases even more rapidly with number of A-lines. When the number of A-lines increases to be 2048, the total time to process multi-functional images using GPU program is smaller than the time of computing intensity image only by purely CPU program.

### 2.3 MF-SD-OCT Processing Steps

#### 2.3.1 Intensity

Calibrating the spectrum on each camera is critical in SD-OCT systems, and even more so for accurate calculation of phase retardation in PS-OCT [55]. The initial wavelength assignments on the cameras were calculated from the spectrometer, similar to a previous method [44]. Next, a correction was applied by inducing a known modulation on the spectrum using a

coverslip [55]. Raw data read from the cameras was resampled uniformly in k-space using the calibrated wavelengths. A depth profile was obtained after a fast Fourier transform (FFT) of the spectrum. The combination of the two polarization channels,  $H_n(z_m)$  and  $V_n(z_m)$ , contributed to the intensity image, where  $H$  and  $V$  distinguish depth profiles from the two cameras respectively,  $n$  is the depth profile number,  $z$  is the depth into the tissue and  $m$  is the pixel number in the depth profile. The intensity was computed as

$$I_n(z_m) = H_n(z_m) \cdot H_n^*(z_m) - V_n(z_m) \cdot V_n^*(z_m) \quad (1)$$

where  $*$  represents the complex conjugate, and displayed using a logarithmic gray scale.

### 2.3.2 Flow

Flow was calculated as the phase difference between two successive complex depth profiles after Fourier transforming the resampled data. Two kinds of flow information can be obtained, bi-directional and phase variance. Bi-directional flow was calculated as the weighted phase difference of two successive depth profiles at corresponding depths. Phase variance was calculated as the weighted square of this phase difference. Since there were two polarization states alternating in the source for neighboring depth profiles, the phase difference at depth  $z_m$  was calculated as phase difference between A-lines having the same incident polarization state:

$$\Delta\phi_{H_n, V_n}(z_m) = \phi_{H_n, V_n}(z_m) - \phi_{H_{n-2}, V_{n-2}}(z_m) \quad (2)$$

The overall phase shift between depth profiles was removed. The phase differences of the last two depth profiles were assumed to be zero. Bi-directional flow and phase variance flow are expressed as Eq. (3) and Eq. (4), respectively [44]:

$$\omega_n(z_m) = \frac{1}{2T} \cdot \frac{|H_n(z_m)|^2 \Delta\phi_{H_n}(z_m) + |V_n(z_m)|^2 \Delta\phi_{V_n}(z_m)}{|H_n(z_m)|^2 + |V_n(z_m)|^2} \quad (3)$$

$$\sigma_n^2(z_m) = \frac{|H_n(z_m)|^2 \Delta\phi_{H_n}^2(z_m) + |V_n(z_m)|^2 \Delta\phi_{V_n}^2(z_m)}{|H_n(z_m)|^2 + |V_n(z_m)|^2} \quad (4)$$

Either bi-directional flow or phase variance are calculated in the real-time processing program depending on user preference. Phase variance was used in the figures in this paper.

### 2.3.3 Phase Retardation

Phase retardation was calculated using the Stokes vector based method [44] in the real-time processing program due to its relatively low computational load. Stokes vectors,  $\mathbf{S}_n(z_m)$ , were calculated from complex depth profiles after FFT,  $H_n(z_m)$ ,  $V_n(z_m)$ , such that

$$\mathbf{S}_n(z_m) = \begin{bmatrix} Q_n(z_m) \\ U_n(z_m) \\ V_n(z_m) \end{bmatrix} = \begin{bmatrix} H_n(z_m) \cdot H_n^*(z_m) - V_n(z_m) \cdot V_n^*(z_m) \\ H_n(z_m) \cdot V_n^*(z_m) + H_n^*(z_m) \cdot V_n(z_m) \\ i(H_n(z_m) \cdot V_n^*(z_m) - H_n^*(z_m) \cdot V_n(z_m)) \end{bmatrix} \quad (5)$$

The position of the sample surface within each depth profile,  $s_n$ , was determined by thresholding the intensity depth profile. The cumulative sample relative optic axis,  $A_i$ , that simultaneously rotates a pair of surface polarization states to states at a particular depth, was determined by

$$A_i(z_m) \parallel (\mathbf{S}_{2i}(s_{2i}) - \mathbf{S}_{2i}(z_m)) \times (\mathbf{S}_{2i+1}(s_{2i+1}) - \mathbf{S}_{2i+1}(z_m)) \quad (6)$$

The phase retardation angle was calculated by the rotation angle from surface state to state at specific depth, which was given by

$$\theta_{2i}(z_m) = \cos^{-1} \left( \frac{|(\mathbf{A}_i(z_m) \times \mathbf{S}_{2i}(s_{2i})) \cdot (\mathbf{A}_i(z_m) \times \mathbf{S}_{2i}(z_m))|}{|(\mathbf{A}_i(z_m) \times \mathbf{S}_{2i}(s_{2i}))| |\mathbf{A}_i(z_m) \times \mathbf{S}_{2i}(z_m)|} \right) \quad (7)$$

$\theta_{2i+1}(z_m)$  can be obtained similarly. The overall phase retardation angle is calculated through a weighted average based on the intensities of the polarization states. Moreover, the effect of noise on the value of  $\theta_{2i+1}(z_m)$  increases as the angle between the rotation axis  $\mathbf{A}_i(z_m)$  and either Stokes states  $\mathbf{S}_{2i}(s_{2i})$  or  $\mathbf{S}_{2i}(z_m)$  decreases. The angle between  $\mathbf{A}_i(z_m)$  and  $\mathbf{S}_{2i}(s_{2i})$  can be calculated from:

$$\sin \theta_{\mathbf{A}_i(z_m), \mathbf{S}_{2i}(s_{2i})} = \frac{|\mathbf{A}_i(z_m) \times \mathbf{S}_{2i}(s_{2i})|}{|\mathbf{A}_i(z_m)| |\mathbf{S}_{2i}(s_{2i})|} \quad (8)$$

The angles between  $\mathbf{A}_i(z_m)$  with  $\mathbf{S}_{2i+1}(s_{2i+1})$  and  $\mathbf{S}_{2i+1}(z_m)$  can be calculated similarly. The overall weight factor can be determined as the product of the sines of the angles between the axis of rotation and the polarization states, which are:

$$W_{2i}(z_m) = I_{2i}(s_{2i}) \sin \theta_{\mathbf{A}_i(z_m), \mathbf{S}_{2i}(s_{2i})} I_{2i}(z_m) \sin \theta_{\mathbf{A}_i(z_m), \mathbf{S}_{2i}(z_m)} \quad (9)$$

$$W_{2i+1}(z_m) = I_{2i+1}(s_{2i+1}) \sin \theta_{\mathbf{A}_i(z_m), \mathbf{S}_{2i+1}(s_{2i+1})} I_{2i+1}(z_m) \sin \theta_{\mathbf{A}_i(z_m), \mathbf{S}_{2i+1}(z_m)} \quad (10)$$

The overall weighted averaged phase retardation angle was determined as:

$$\eta_i(z_m) = \frac{W_{2i}(z_m) \theta_{2i}(z_m) + W_{2i+1}(z_m) \theta_{2i+1}(z_m)}{W_{2i}(z_m) + W_{2i+1}(z_m)} \quad (11)$$

### 3. Results

#### 3.1 System characterization

Basic system characterization was done in a similar fashion to that of Yun et al [56]. The power incident on the sample surface is 6mW. The photon-to-electron conversion efficiency of the spectrometer is 63% for both cameras. The theoretical imaging depth is 3.4mm calculated from spectrometer, the actual measured imaging depth in air is 3 mm, thus 2mm in biological tissue if refractive index is 1.5. The SNR ranges from 51dB at the surface to 40dB at 3mm measured by using a mirror as sample, the sensitivity drop-off is less than 10dB from surface to 2.5mm in air. The axial resolution is 8 $\mu$ m up to a depth of 1mm and 11 $\mu$ m at a depth of 3mm measured by a mirror.

While a computationally-efficient Stokes vector approach was implemented in the acquisition software, the general appearance of PS-OCT images were compared to a more rigorous Jones matrix-based method in post-processing. This Jones matrix approach has the advantage of determining relative optic axis, phase retardation, and diattenuation simultaneously [57]. Characterization data was obtained using a polarizing film for diattenuation and a waveplate for phase retardation. The polarizing film had a diattenuation of 1 and the wave plate had a round-trip phase retardation of 166° at 1300nm. The round-trip diattenuation and phase retardation were calculated for these two samples separately using the Jones matrix method [57]. The measured round-trip diattenuation using one polarizing film at different set orientations is  $0.98 \pm 0.002$  (Fig. 5(a), red dots, PF1). The measured round-trip phase retardation of the wave plate is  $167.5 \pm 2.5^\circ$  (Fig. 5(b), red dots, WP). The measured optic axis orientation is shown in Fig. 5(c) with red dots. The measured round-trip diattenuation, round-trip phase retardation and optic axis orientation match the theoretical values. A polarizing film with diattenuation of 0.15 (measured as  $0.15 \pm 0.022$  shown in Fig. 5(a), blue squares, PF2) was placed on top of the same wave plate with their optic axes aligned. Measured round-trip phase retardation and diattenuation after placing the polarizing film are  $167.4 \pm 5.2^\circ$  (Fig. 5(b), blue squares, PFWP) and  $0.179 \pm 0.085$  (Fig. 5(a), black

triangles, PFWP) respectively. The measured optic axis is shown in Fig. 5(c) with blue squares. Both sets of measurements (the separate samples and combined sample) agree well with theoretical values. A combined sample comprised of a polarizing film and a wave plate demonstrates that phase retardation, diattenuation, and optic axis can be measured using the Jones matrix method.

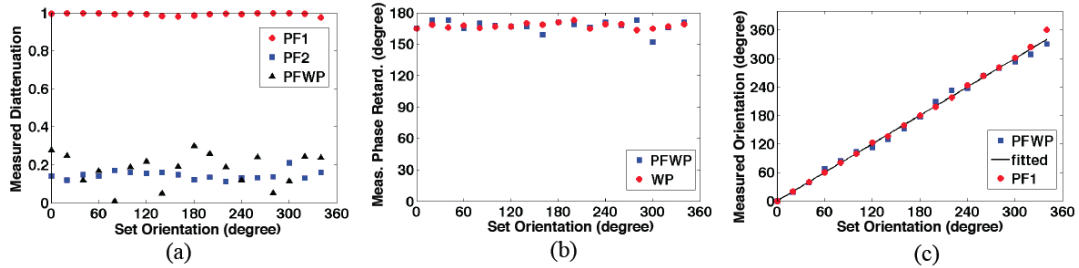


Fig. 5. (a) Measured round-trip diattenuation of polarizing films with diattenuation of 1 (PF1, red dots) and 0.15 (PF2, blue squares) with set orientation; (b) measured round-trip phase retardation of a single wave plate (WP, red dots) and combined sample with a polarizing film with diattenuation 0.15 atop of same wave plate (PFWP, blue squares) with set orientation; (c) measured optic orientation of single polarizing film with diattenuation of 1 (PF, red dots) and combined sample with a polarizing film atop of wave plate (PFWP, blue square).

It is known that muscle tissue is highly birefringent and adipose tissue is not [58,59]. Chicken muscle and adipose were imaged under PS-OCT. Post processed intensity and PS-OCT images of adipose and muscle tissue are shown in Fig. 6. It is clear that adipose tissue is not birefringent and muscle is highly birefringent, as demonstrated by the striped pattern in the PS-OCT image. Phase retardation was quantified by averaging the phase retardation over regions of muscle and adipose tissue starting from sample surface. A linear fit was applied to the resulting curve and the slope extracted as a measurement of phase retardation per unit depth. The averaged slope for adipose and muscle are shown in Fig. 6(g) and 6(h). The phase retardation per unit depth is  $0.8821 \pm 0.045^\circ/\mu\text{m}$  for muscle tissue and  $-0.026 \pm 0.08^\circ/\mu\text{m}$  for adipose tissue. As proof that the above characterization can accurately extract phase retardation amidst the existence of diattenuation, the polarizing film with diattenuation of 0.15 was put on top of the sample of chicken muscle and imaged as a single sample. Extraction of phase retardation requires identical eigenvectors determined from the Jones matrices of the sample and film. The polarizing film was carefully put atop of the chicken muscle with their optic axes aligned in the same direction. Figure 6(c), 6(f) and 6(i) show the intensity image, PS-OCT image and averaged phase retardation per unit depth. The measured average phase retardation per unit depth is  $0.907 \pm 0.07^\circ/\mu\text{m}$ , which agrees well with the previous measurement. The PS-OCT characterization and imaging results demonstrate the ability of our multi-functional SD-OCT system to maintain good sensitivity while operating the cameras at their maximum line rate of 45 kHz.

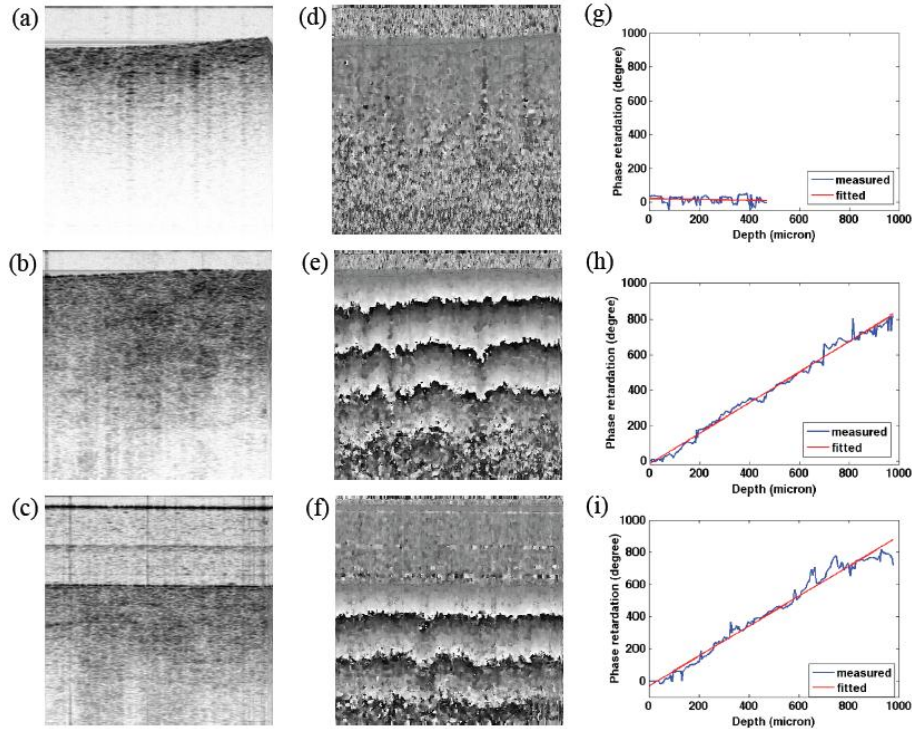


Fig. 6. Intensity, PS-OCT images, and averaged phase retardation along depth for chicken adipose tissue (a, d, g), muscle (b, g, h) and a polarizing film putting on top of the same muscle (c, f, i). After putting polarizing film on the same piece of chicken muscle, PS-OCT can still be extracted correctly as shown in (f). Phase retardation slope ( $0.907 \pm 0.07^\circ/\mu\text{m}$ ) after placing polarizing film (i) is similar to the phase retardation slope ( $0.8821 \pm 0.045^\circ/\mu\text{m}$ ) without putting polarizing film shown in (h). The width and depth of the images were 2mm.

### 3.2 Imaging and video recording of a Horseshoe crab eye

A live horseshoe crab eye was imaged *in vivo* using the CPU-GPU hybrid acquisition program. A horseshoe crab lateral compound eye is comprised of hundreds of thousands of small segments called ommatidia. The compound eye was scanned in a volume of  $0.8 \times 0.8 \times 2\text{mm}^3$ . Only the cross-sectional intensity and its *en face* images were calculated and displayed to test the processing program, every frame acquired was processed and displayed. Three different volume sizes were tested, which are:  $256 \times 50 \times 512$  (12,800 A-lines/volume),  $512 \times 50 \times 512$  (25,600 A-lines/volume),  $1024 \times 50 \times 512$  (51,200 A-lines/volume). These volumes were acquired and visualized at 3volumes/second, 3volumes/2seconds, 4volumes/5seconds, respectively.

The representative frames of videos recorded for above volume sizes are shown in Fig. 7 (a, [Media 1](#)), (b, [Media 2](#)), (c, [Media 3](#)) respectively. The *en face* depth was  $380 \mu\text{m}$  from eye surface. Figure 7 (c, [Media 4](#)) shows a representative frame of video for volume size of  $512 \times 50 \times 512$  with *en face* depth  $70 \mu\text{m}$  deeper. The intensity cross-sectional image is on the left and *en face* image on the right in each frame. In Fig. 7(a), arrows in cross-sectional image point to crystal cone walls of ommatidia, and arrows in *en face* image indicate hexagonal ommatidia. The arrows in cross-sectional image of Fig. 7(b) show the membrane fenestrate at the end of ommatidia. Moving  $70 \mu\text{m}$  deeper in Fig. 7(d), more ommatidia are seen on right section of *en face* image as indicated by arrows. A single ommatidium has a diameter of about  $200 \mu\text{m}$  from the *en face* image.

The intensity images were updated on a frame-to-frame basis, and the *en face* image was updated simultaneously line by line. The program is capable of processing and updating

image frames quickly enough for the *en face* image of the volume to be updated at a rate of 3 volumes/second for voxel size of  $256 \times 50 \times 512$ .

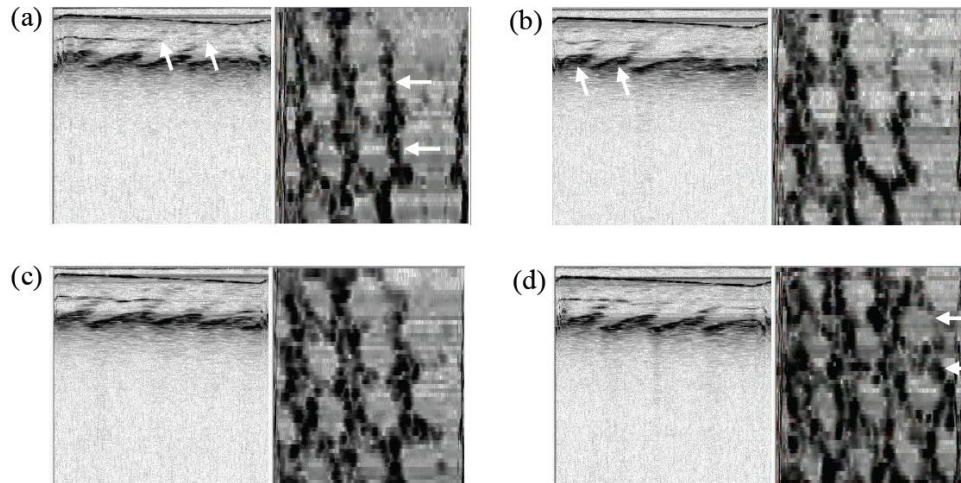


Fig. 7. Live imaging of a horseshoe crab lateral compound eye, cross-sectional intensity image (0.8mm in width and 2mm in height) is on left and *en face* image (both width and height are 0.8mm) is on right. (a)  $256 \times 50 \times 512$  voxels: *en face* depth is about  $380\mu\text{m}$  deep from eye surface (Media 1); (b)  $512 \times 50 \times 512$  voxels (Media 2): same *en face* depth with (a); (c)  $1024 \times 50 \times 512$  voxels (Media 3): same *en face* depth with (a); (d)  $512 \times 50 \times 512$  voxels, *en face* depth is  $450\mu\text{m}$  from eye surface (Media 4). The arrows in cross-sectional image of (a) indicate walls of crystal cones, arrows in *en face* images of (a) and (d) are pointing to hexagonal ommatidia. Arrows in cross-sectional image of (b) show membrane fenestrates at the end of ommatidia.

### 3.3 Imaging and video recording of chicken muscle

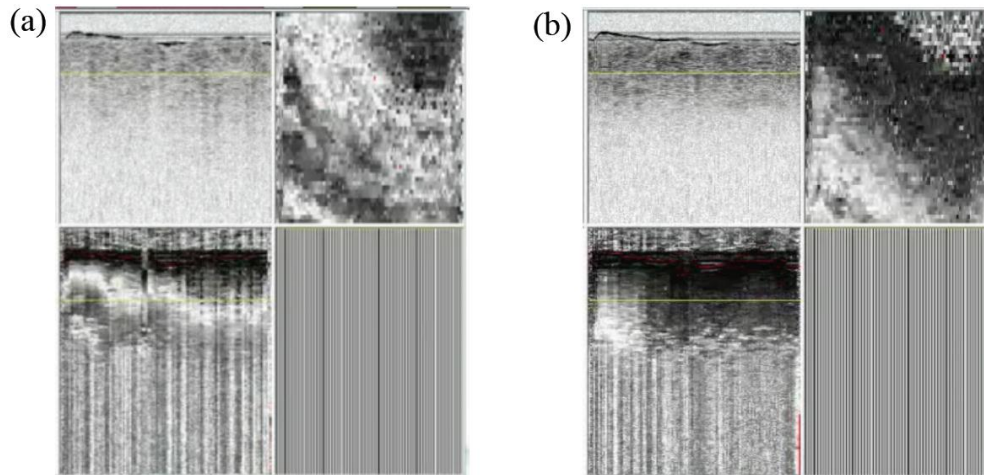


Fig. 8. Imaging and video recording of chicken muscle (Media 5), with heated applied to a lateral position corresponding to the top right corner: (a) A representative frame of the video when heat started transmitting from top right corner; (b) A representative frame when heat propagated to surrounding area. In both (a) and (b), top left, the four views are: cross-sectional intensity image (top left,  $1.3\text{mm} \times 2\text{mm}$ ), phase retardation image (bottom left,  $1.3\text{mm} \times 2\text{mm}$ ), *en face* phase retardation image (top right,  $1.3\text{mm} \times 1.3\text{mm}$ ). Cross-sectional flow image display on the bottom right was deactivated during video recording as there was no live flow in this piece of chicken muscle.



In order to test the phase retardation computation of the CPU-GPU hybrid acquisition program, a piece of chicken muscle was imaged as heat was applied to the top right corner of imaging area. The scanned volume size is  $1.3 \times 1.3 \times 2 \text{ mm}^3$  ( $256 \times 50 \times 512$ ).

The fast computation speed (1.7 seconds/volume) allowed visualization of the birefringence changes during propagation of thermal injury in the volume. Figure 8(a) and 8(b) are two representative frames of chicken muscle during heating process (Media 5). In each frame, the image views are cross-sectional intensity (top left), phase retardation (bottom left), and *en face* phase retardation (bottom right) images. The yellow lines in the cross-sectional images indicate the depth of *en face* image. The cumulative phase retardation in *en face* image at chosen depth is roughly equal at the start of the recording as the sample was uniformly birefringent. As localized heat was applied to one corner, the cumulative phase retardation at the *en face* depth visualized changes non-uniformly as shown in Fig. 8(a). In the cross-sectional phase retardation image, right half started losing more birefringence than left. As heat continued propagating to surrounding area, chicken in heated area gradually lost birefringence. In Fig. 8(b), the *en face* image showed a larger area of black, indicated low levels of cumulative phase retardation; this is reflected in the cross-sectional images, as the portion of the sample with less applied heat retained greater amount of birefringence than that where the heat was applied.

### 3.4 Imaging and video recording of microfluid flow

A microfluidic device was imaged in order to test flow computation (phase variance) of the CPU-GPU hybrid program. The program was set to process every other frame (1028 A-lines by 512 pixel) acquired such that while 200 frames/volume were acquired, only 100 frames/volume were processed and displayed in the GUI. The scanned volume size was  $1.8 \text{ mm} \times 1.8 \text{ mm} \times 2 \text{ mm}$  ( $1028 \times 100 \times 512$ ), and it took 5 seconds to update one volume. As shown in Fig. 9(a), a micro channel with 600  $\mu\text{m}$  diameter was carved on apolydimethylsiloxane (PDMS) sheet and fixed to a glass slide with 1.1 mm thickness. One end of the micro channel was connected to a syringe through a plastic tube and a needle, the other end of the micro channel was connected to a petri dish containing diluted intralipid through a tube. The syringe could pump in and out diluted intralipid through the micro channel by pushing or pulling the syringe. The microfluidic device was imaged with glass slide surface close to the incident beam. Figure 9(b) is a representative frame of the video recording fluid change, the four views are cross-sectional intensity image (top left,  $1.8 \text{ mm} \times 2 \text{ mm}$ ), *en face* flow image (top right,  $1.8 \text{ mm} \times 1.8 \text{ mm}$ ), cross-sectional flow image (bottom right,  $1.8 \text{ mm} \times 2 \text{ mm}$ ), cross-sectional phase retardation image (bottom left, blocked during video recording). In order to focus the light at the microfluidic channel, the glass slide was slightly shifted towards to the complex positions to portray a more intense image of the microfluidic channel on the display. The top surface of the glass slide was indicated by arrow 1 in Fig. 9(b), and arrow 2 showed bottom layer of glass slide sticking with PDMS. In cross-sectional flow image, the white region shows the spatial position where there was flow change, the black rings indicate phase wrapping as phase change went beyond  $\pi$ . Turbulent flow was observed shown as two regions of flow, similar to the observation by Bonesi [60].

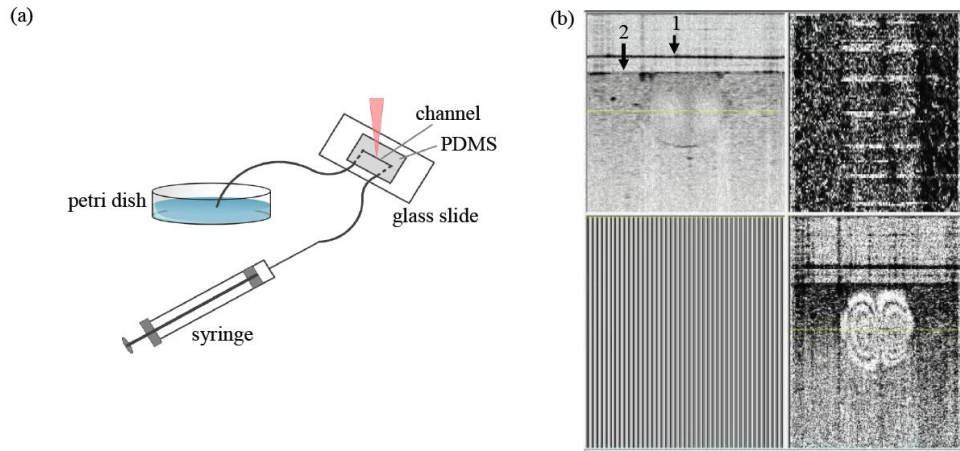


Fig. 9. (a) Set-up of the microfluidic device: the micro channel with  $600\ \mu\text{m}$  diameter was carved on a PDMS sheet and fixed to a glass slide. Top surface of glass slide was close to incident beam. Inlet of micro channel was connected to a syringe through a plastic tube and a needle, the outlet of micro channel was connected to a petri dish containing diluted intralipid through a plastic tube. (b) A representative frame of imaging flow change in the microfluidic device (Media 6): the four views are cross-sectional intensity image (top left,  $1.8\text{mm} \times 2\text{mm}$ ); *en face* flow image (top right,  $1.8\text{mm} \times 1.8\text{mm}$ ); cross-sectional flow image (bottom right,  $1.8\text{mm} \times 2\text{mm}$ ); display of cross-sectional phase retardation view on the bottom left was deactivated as PDMS is for the purpose of testing intensity and flow in this section. The glass slide was slightly shifted to the conjugate complex positions to portray a more intense image of microfluidic channel in the display. Arrow 1 indicates the top surface of glass slide and arrow 2 points to bottom layer of glass slide which is fixed to PDMS. In flow cross sectional image, we see the ring shape white and dark pattern caused by phase wrapping, and turbulence was seen because of high speed pushing and resistance in the channel.

### 3.5 Multi-functional imaging of a mouse brain

A mouse brain with a thin skull preparation was imaged *in vivo* by using this multi-functional SD-OCT system. The CPU-GPU hybrid processing program is capable of processing and displaying every other image frame ( $512\ \text{pixel}$  by  $2048\ \text{A-lines}$ ) and update the intensity, phase retardation and flow images, as well as the *en face* image of the selected image type at the selected depth (10 frames per second). The scanning volume was composed of 400 frames, processing every other image frame results in 200 frames displaying in the volume ( $2\text{mm} \times 2\text{mm} \times 2\text{mm}, 2048 \times 200 \times 512$ ).



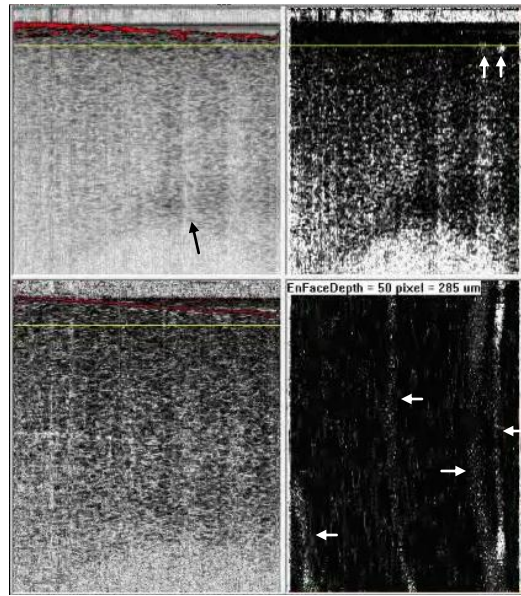


Fig. 10. A representative frame of *in vivo* imaging a mouse brain with thin skull (Media 7): cross-sectional intensity image (top left), cross-sectional flow image (top right), cross-sectional phase retardation image (bottom left) and *en face* flow image (bottom right). The image sizes are all 2mm by 2mm. The updating rate of the video is 10 frames (512 pixel by 2048 A-line) per second. The red spots in intensity image indicate signal saturation, red line in phase retardation image shows surface line of sample, the yellow lines in all three cross-sectional images indicate the *en face* depth. The arrow in intensity image point to corpus callosum, arrows in cross-sectional flow image show the spatial cross-section positions of two blood vessels, arrows in *en face* flow image show four blood vessels lying on the *en face* depth of the scanning volume.

Figure 10 shows a snapshot of the 4 image views of the GUI during *in vivo* imaging of a mouse brain with a thin skull preparation (Media 7). The four views are cross-sectional intensity image (top left), flow image (top right), phase retardation image (bottom left), and *en face* flow image (bottom right) respectively, the image sizes are all 2mm × 2mm. The red spots in intensity image indicate signal saturation at the surface, the red line in polarization image shows the surface of the sample. The yellow line in intensity, flow and phase retardation indicates the depth of *en face* image in volume. This depth was also shown in *en face* image as number of pixels and microns. In the intensity image, corpus callosum was visible with higher scattering indicated by arrow. The gray matter was weakly birefringent thus it showed generally dark in phase retardation image. The cross-sectional flow image captured the spatial cross-section positions of two blood vessels in this frame indicated by arrows. In the *en face* flow image after finishing scanning the whole volume, four blood vessels were visible at the chosen *en face* depth. As the blood vessels did not lie exactly on the same *en face* plane, that flow signal was weaker or stronger for part of blood vessels at this specific depth.

#### 4. Conclusion

In conclusion, we have demonstrated a GPU-accelerated multi-functional SD-OCT system at 1300nm. The program is capable of processing and displaying every frame for intensity images (512 pixel by 2048 A-lines) and its *en face* images (100 images by 2048 A-lines) at a rate of 20 frames per second using GPU-accelerated processing algorithms. The program is capable of processing and displaying simultaneous intensity and flow images (512 pixel by

2048 A-lines), phase retardation images (512 pixels by 1024 A-lines) and *en face* images (100 images by 2048 A-lines) at 10 frames per second. The data processing time of the GPU-accelerated program is five times faster than the previous CPU-based processing program. Additionally, it is first time that the characterization of diattenuation and phase retardation for PS-OCT systems has been done simultaneously from a single sample using the Jones matrix method. The characterized diattenuation, phase retardation and optic axis match well with the theoretical values. Our imaging results of a chicken muscle demonstrate that phase retardation can be extracted correctly by Jones matrix in the presence of diattenuation. A horseshoe crab eye was imaged *in vivo* and four videos with varying volume sizes (12800, 25600, 51200A-lines/volume) were recorded which gave volume update rate of 3volumes/second, 3volumes/2seconds, 4volumes/5seconds, respectively. Structures of ommatidia were observed from the *en face* images and can be identified quickly due to the rapid visualization capability of our system. The fast visualization capability allowed visualization of large-scale birefringence changes due to localized heating of a chicken sample. The *en face* phase retardation image clearly showed the heat propagation from top right corner to surrounding area where showed black color with birefringence loss. A microfluidic device with a channel of 600 $\mu$ m in diameter was used to test the flow computation, the cross-sectional flow image showed the phase variance change, and turbulent flow was observed. The frequency of pushing and pulling syringe to pump diluted intralipid through the micro channel was visible in *en face* image. Finally, a mouse brain with a thin skull preparation was imaged with all image views (intensity, phase retardation, flow, *en face* flow) updating at a rate of 10 frames per second with the *en face* flow view displaying blood vasculature and demonstrated our ability to do rapid identification of structures in OCT images.

### **Acknowledgments**

We acknowledge the support from National Institute of Health (R00EB 007421) and the Department of Bioengineering at UCR. We also wish to thank Mike Hsu and Jenny Szu for the assistance on the animal protocol and mouse preparation, and Md. Rezuanul Haque for help with horseshoe crab eye imaging. B.H. Park's email address is [hylepark@engr.ucr.edu](mailto:hylepark@engr.ucr.edu)